Generation of self-stabilized chirped dissipative Kerr solitons in the normal-dispersion regime of a Si$_3$N$_4$ microring resonator with built-in spectral filtering

Sauradeep Kar[*] and Shailendra K. Varshney [†]

Department of Electronics and Electrical Communication Engineering, Indian Institute of Technology, Kharagpur 721302, India

Temporal dissipative Kerr solitons (DKSs) and their frequency counterparts, Kerr frequency combs (KFCs), have been extensively explored in the anomalous dispersion regime for both continuous wave (CW) and pulse-pumped microresonators. Compared to the CW pumping, the pulsed pump scheme has been shown to produce DKSs with higher robustness. Recently DKS states have also been explored in the normal dispersion regime as well. In this work, we demonstrate a stable single DKS state originating from a normal dispersion regime of a silicon nitride (Si$_3$N$_4$) racetrack microring resonator with a built-in spectral filter for a chirped super-Gaussian pulsed pump. Numerical simulations aided with analytically derived formulations indicate that a stable square-shaped chirped DKS with a broad KFC can be generated. The proposed scheme also enhances the stability of the single-chirped DKS state. The interplay of input chirp along with the spectral filtering effect causes the stable single DKS to be trapped conveniently to the center of the driving pulse background. We believe that the findings along with derived analytical formulations will be useful and might find applications in communication, spectroscopy, optical tweezers, and more general all-optical manipulation of light pulses.

I. INTRODUCTION

Temporal dissipative Kerr solitons (DKSs) are self-sustained, ultrashort optical pulses generated in dispersive and coherently driven Kerr nonlinear resonators [1]. DKSs generated by the composite balance between group velocity dispersion (GVD) and Kerr nonlinearity on one hand along with cavity loss and external driving input pump on the other hand [2,3] are inherently robust [4]. To date, DKSs have been demonstrated in all-fiber [5], on-chip [6], and bulk resonator [7] platforms. In sharp contrast to the dissipative solitons (DSs) in mode-locked lasers [8], DKSs manifest as coherent and equidistant spectral lines called Kerr frequency combs (KFCs) in the spectral domain [9] which span over a wide spectral bandwidth. KFCs enjoy diverse applications including optical frequency synthesizers [10,11], all-optical buffering [12], spectroscopy [13], optical tweezers [14], and many more. In addition to bandwidth, sustained KFCs generated from single stable DKS states are essential for several applications [15].

Traditional single DKS and hence KFC are generated in the anomalous dispersion regime [16], where such DKS pulses mostly remain limited in pulse duration and peak energy [17,18]. On the other hand, DSs in mode-locked lasers reflect a unique feature of frequency chirping in contrast to traditional solitons in optical fibers [19]. This makes bright DSs accessible in the normal dispersion regime through spectral filtering [20]. Motivated by the concept of frequency-chirped DSs in mode-locked lasers, researchers are exploring the possibility of stable DKS generation in the normal dispersion regime as well, through the composite balance between frequency chirp, spectral filtering, and dispersion. The first exploration of the spectral filtering concept was in a normal dispersion microresonator with wavelength-dependent quality factor [21]. Recently, spectral filtering has been demonstrated to generate highly positive frequency chirped DKSs in a normal dispersion fiber resonator [22]. Besides this, versatile resonator architectures, showing normal dispersion, have been proposed to study the complex dynamics of a wide range of pulse regimes including dark solitons [23,24], switching waves [25,26], Raman solitons [27–29], and others. In addition, bright DKS structures have also been reported in a dispersion-shifted fiber (DSF) based ring resonator [30] pumped in the normal dispersion regime. The significant presence of higher-order dispersion effects is the predominant underlying mechanism behind the generation of such DKSs.

Generally, DKSs in microring resonators are driven by continuous wave (CW) pump sources [15,31]. The CW driving signal forms a homogeneous background, which gives rise to sech-shaped DKS that may rest at any random position within the homogeneous background. Thus, without any active control [32–34] or passive modulation [35,36] the temporal position of the DKS remains stochastic in the case of CW pumps. Also, the temporal overlap between the DKS and CW pump is less, which leads to inefficient pump-to-soliton conversion [37,38]. To circumvent these disadvantages, two alternative methods have been demonstrated in the literature for generating stable bright DKSs [15]. These include the usage of mutually coupled multiple resonators [39] and the synchronized pulse pumping scheme [40]. The former method involves complicated ring geometries, making the latter method much simpler and straightforward. The amplitude

---

*dhruba12@iitkgp.ac.in

†skvarshney@ece.iitkgp.ac.in

033502-1

inhomogeneity of the pulse driving scheme aids in trapping the generated DKS at deterministic locations on top of the pulsed background [41]. Such trapping locations depend on the driving pulse energy [42]. Recent studies have further explored the efficient control of trapping locations and soliton dynamics upon pumping the resonator in the anomalous dispersion regime by a chirped phase-modulated pulsed driving field [43]. Also, a recent work [44] has reported unique signatures of square-shaped DKSs with a flat spectrum in a normal dispersion fiber resonator with a pulse pump and spectral filtering.

The present paper proposes and theoretically demonstrates the generation of stable single DKS states in an on-chip racetrack microring resonator (RMRR) with spectral filtering and the chirped pulsed pump. The RMRR configuration is similar to our previous work [15], but in addition consists of a spectral filtering element. For the proposed RMRR, a comparative study of the DKS states has been conducted in both the anomalous and normal dispersion regimes without and with a spectral filter, respectively. The unchirped Gaussian and chirped super-Gaussian pulsed driving fields have been used in numerical simulations. Spectral filtering along with chirped phase modulation in the normal dispersion regime have yielded characteristic square-shaped stable single DKS states with high power. Through steady-state calculations, it has been predicted that the region of stable chirped-DKSs increases with the higher chirp. The numerical simulations have been carried out with the well-known Lugiato-Lefever equation (LLE) with spectral filtering (called LLE-F) and have been verified by the Ikeda-map approach. Further, the proposed model aids in an improved efficiency towards trapping of the generated DKS compared to recent studies [43]. The extensive mathematical framework reported in this work might help in understanding the spectral and temporal dynamics of pulsed resonator systems.

II. SOLUTIONS OF LLE AND LLE-F WITH PULSE PUMPING

A. Pulse pumping in anomalous dispersion

The temporal DKS state and the KFCs have been simulated by the well-known driven and damped nonlinear Schrödinger equation, which describes the mean-field cavity dynamics. The LLE [45–47] is reproduced for the pulse pumping regime as [41,46]

$$t_R \frac{\partial E}{\partial t} = \left[-\left(\frac{\alpha + \kappa}{2} \right) - i\delta_0 + iL \sum_{m \geqslant 2} \frac{\beta_m}{m!} \left(i \frac{\partial}{\partial \tau} \right)^m \right.$$
$$\left. - \Delta t \frac{\partial}{\partial \tau} + i\gamma L |E|^2 \right] E + \sqrt{\kappa} E_{\text{in}}(\tau), \quad (1)$$

where

$$E_{\text{in}}(\tau) = E_{\text{in}} \exp \left(-\frac{\tau^2}{2\tau_g^2} \right). \quad (2)$$

Here t_R denotes the round-trip time, and $E(t, \tau)$ and $E_{\text{in}}(\tau)$ represent the intracavity and pulsed pump fields, respectively. The slow time t denotes the time for field confinement inside

the resonator following the photon lifetime. The fast time τ indicates the behavior of the temporal envelope of the signal that moves with the group velocity. The mathematical relation $E(t = mt_R, \tau) = E^{(m)}(0, \tau)$ correlates the slow and fast times, where the index m indicates the total number of round trips traversed by the circulating field in the cavity, δ_0 denotes the cavity phase detuning, which is given as $\delta_0 = t_R(\omega_n - \omega_0)$, where ω_0 and ω_n are the angular frequencies of the pump and nth resonance mode, respectively. α, κ, β_m, and γ are the power loss per round trip, coupling coefficient, mth-order dispersion coefficient, and nonlinear coefficient, respectively. L denotes the circumference of the cavity. Δt is the desynchronization parameter that symbolizes the temporal drift of the pump pulse repetition rate with respect to the resonator's free spectral range (FSR), $\text{FSR} = \frac{1}{t_R}$, and is written as $\Delta t = t_R - t_P$, where t_P is the pump pulse repetition rate. E_{in} is the peak driving amplitude and $2\tau_g$ is the full width at half maximum (FWHM) of the pump pulse in the temporal domain. The normalized parameters are

$$\alpha' = \frac{\alpha + \kappa}{2}, \quad t' = \alpha \frac{t}{t_R}, \quad \tau' = \tau \sqrt{\frac{2\alpha'}{|\beta_2|L}},$$

$$E' = E \sqrt{\frac{\gamma L}{\alpha'}}, \quad S(\tau') = E_{\text{in}}(\tau') \sqrt{\frac{\gamma L \kappa}{\alpha'^3}}, \quad D = \frac{\delta_0}{\alpha'},$$

$$d = \Delta t \sqrt{\frac{2\Im}{(|\beta_2|L\pi)}}, \quad \tau'_g = \tau_g \sqrt{\frac{2\alpha'}{|\beta_2|L}},$$

where $\Im = \frac{\pi}{\alpha}$ is the finesse of the resonator. Equation (1) can be recast in the normalized form as

$$\frac{\partial E'}{\partial t'} = \left[-1 + i(|E'|^2 - D) - d \frac{\partial}{\partial \tau'} + i \frac{\partial^2}{\partial \tau'^2} \right] E' + S(\tau').$$
$$(3)$$

Equation (3) solved with steady-state ($\frac{\partial E'}{\partial t'} = 0$) and homogeneous ($\frac{\partial E'}{\partial \tau'} = 0$) criteria results in the following cubic equation [42,46]:

$$X = Y^3 - 2Y^2 + (D^2 + 1)Y, \quad (4)$$

where $X = |(S(\tau'))_{\text{avg}}|^2$ and $Y = |E'|^2$. Three sets of intracavity field solutions can be acquired from Eq. (4): (1) unconditionally homogeneous stable steady-state solutions, (2) unconditionally homogeneous unstable solutions, and (3) conditionally homogeneous stable (oscillatory) solutions. The phenomenon of modulation instability [48], where a perturbation develops on top of the steady-state background in both anomalous and normal dispersion regimes [46,48], generates the oscillatory solutions. When Eq. (4) is treated as a second-order polynomial in D, it can be solved for three classes of solutions:

$$D = Y \pm \sqrt{\frac{X}{Y} - 1}. \quad (5)$$

In this section, the LLE simulations are carried out at a pump wavelength of 1560 nm. The same RMRR configuration of [15] has been considered for simulation purposes. The resonator has β_2 of -174.9 ps^2/km and t_R of 3.687 ps at the

TABLE I. Simulation parameters for DKS in Sec. II A.

Parameter	Value
Pump wavelength (λ_0)	1560 nm
Round-trip time (t_R)	3.687 ps
Round-trip loss (α)	0.0034
Coupling coefficient ($\kappa_{\mathrm{normalized}}$)	0.0044538
Second-order GVD (β_2)	-174.9 ps^2/km
Third-order dispersion (TOD) (β_3)	-0.318 ps^3/km
Nonlinear parameter (γ)	0.65 W^{-1}m^{-1}
Input power (P_{in})	132 mW
Desynchronization(Δt)	0.026 ps

pump wavelength. The input pulse is Gaussian according to Eq. (2) with a temporal FWHM pulse width ($2\tau_g$) of 3.56 ps, and period t_P of 3.661 ps yielding a desynchronization (Δt) of 0.026 ps. Although soliton generation is easily feasible when the repetition rate of the input pump synchronizes with that of the cavity [30,43], still the value of Δt in this work is small enough to ensure proper generation of DKS state [41]. The input pump power $P_{\mathrm{in}} = |E_{\mathrm{in}}|^2$ of 132 mW is scanned over a range of detuning values to explore the behavior of the intracavity field at different homogeneous steady-state (HSS) solution regimes of the LLE. All other parameters are the same as mentioned in [15] (the parameters have been further summarized in Table I). The solutions of Eq. (5) for the stable, unstable, and oscillatory intracavity fields have been depicted in Fig. 1 with black filled circles, red asterisks, and blue (light gray) open circles, respectively. The LLE has been solved numerically with the well-known split-step Fourier method [48] to obtain steady-state solutions for three regimes. Four representative solutions in the respective regimes have been depicted in the inset. Initially, in the stable regime, the formation of a multi-DKS state is represented (inset I) [40]. A multi-DKS builds on top of the input pulse background. Oscillatory solutions are observed with an increase in detuning parameter. In inset II an oscillatory solution with a Turing pattern [49,50] like behavior is depicted. Interestingly, upon pumping the cavity with pulses, the duration of the Turing
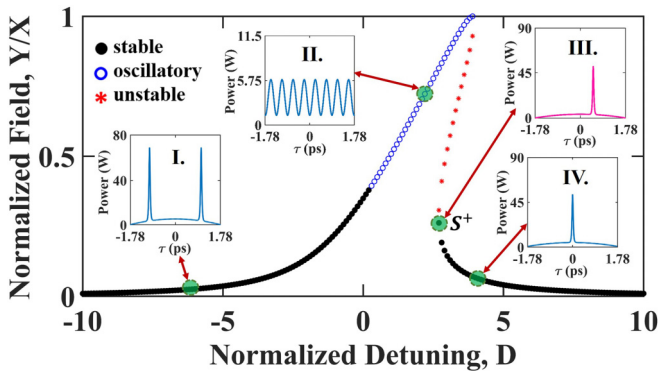

FIG. 1. Location of stable nontrivial solutions of Eq. (5) in the parameter space defined by the tilt response. The stable, unstable, and oscillatory solutions are marked by black-filled circles, red asterisks, and blue (light gray) open circles, respectively. Pulse profiles of four representative solutions in the respective regimes are given as insets.

pattern is the same as the input pulse width ($2\tau_g$). Again, in the lower branch of the tilt response, a stable single DKS state atop the input pulse profile is observed (inset IV). It should be noted that the power of this single DKS state is lower than the multi-DKS. If the input power is increased close to the up-switching point (marked by S^+) [12], the DKS drifts from the center, as shown in inset III. This is consistent with findings reported in [42].

B. Bright soliton generation in normal dispersion

In general, dark solitons are generated in normal dispersion regime [51]. However, to observe bright solitons in the normal dispersion regime, a spectral filtering effect can be added to the resonator [52], which eventually produces chirped DKS [22,52]. The spectral filtering yields the following form of the driven and damped nonlinear Schrödinger equation for the MRR, known as LLE-F [52]:

$$t_R \frac{\partial E}{\partial t} = \left[-\left(\frac{\alpha + \kappa}{2} \right) - i\delta_0 + L\left(-i\frac{\beta_2}{2} + \frac{1}{f^2} \right) \frac{\partial^2}{\partial \tau^2} \right.$$

$$\left. - \Delta t \frac{\partial}{\partial \tau} + i\gamma L|E|^2 \right] E + \sqrt{\kappa} E_{\mathrm{in}}(\tau), \qquad (6)$$

where f is the spectral filter bandwidth, and the rest of the symbols have their usual meaning. Upon normalizing Eq. (6), and normalizing f by the factor $f_{n0} = f\sqrt{L|\beta_2|}$, $\frac{f_{n0}^2}{L} = \Omega^2$, the following equation is obtained:

$$\frac{\partial E'}{\partial t'} = \left[-1 + \left(-i + \frac{1}{\Omega^2} \right) \frac{\partial^2}{\partial \tau'^2} \right.$$

$$\left. + i(|E'|^2 - D) - d\frac{\partial}{\partial \tau'} \right] E' + S(\tau'), \qquad (7)$$

where the symbols have their usual meanings. Here the pump wavelength is 1029.7 nm where the resonator geometry (the same as in Sec. II A and [15]) exhibits a normal second-order GVD (β_2) of 22 ps^2/km and the t_R is 3.717 ps. Simulations have been carried out using a filter bandwidth of 10.475 nm at the pump wavelength. The filter's spectral bandwidth f is calculated according to scaling laws defined for chirped DKS in [52]. The same input Gaussian pulse, as in Sec. II A, has been used with a desynchronization (Δt) of 0.056 ps and a fixed input pump power, $P_{\mathrm{in}} = 100$ mW. The location of the solutions in the parameter space defined by the steady-state homogeneous tilt response of Eq. (7) is shown in Fig. 2 for a range of detuning values. In the stable solution regime, dark solitons [51] (inset I) with a smooth profile are obtained. In the oscillatory regime, bright DKS with oscillatory profile (inset II) is obtained, similar to the chirped DKS profile reported in [52]. Thus, spectral filter bandwidth f plays the most important role in generating bright solitons in the normal dispersion regime [22]. However, it should be noted that the power content of such oscillatory chirped bright DKSs is low.

III. PROPOSED MODEL AND RESULTS

Note that chirped DKSs were reported in a fiber cavity with normal dispersion and an all-fiber format spectral filter [22],
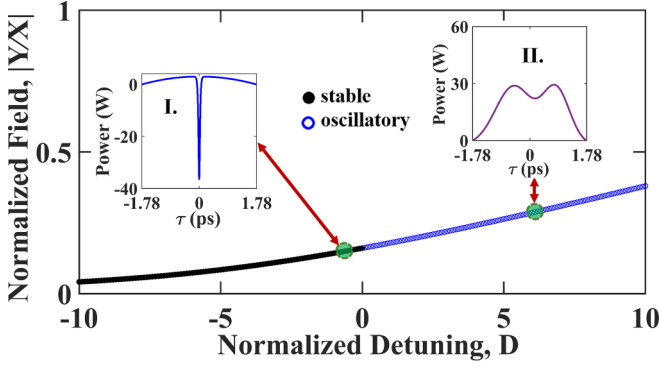
FIG. 2. Location of stable nontrivial solutions of Eq. (7) in the parameter space defined by the tilt response. The stable and oscillatory solutions are marked by the black filled circles and blue (light gray) open circles, respectively. Pulse profiles of two representative solutions in the respective regimes are given as insets.

where the fiber cavity was pumped with nanosecond pulses. In contrast to the reported work [22], the present scheme demonstrates chirped DKSs through a normal dispersion on-chip MRR with a built-in integrated spectral filter. The MRR with spectral filter is driven by chirped super-Gaussian ps pulses. Through the homogeneous steady state analysis of the LLE-F, the present work shows the interplay between input chirp, spectral filtering, and normal dispersion can lead to interesting temporal and spectral signatures of the single DKS, and the same can be trapped at the center of the driving pulse background.

A. Proposed method of chirped pulse pumping

The schematic top view of the proposed RMRR configuration used in this work is depicted in Fig. 3(a). The cross-sectional view is shown in the inset. The RMRR is similar to [15] with a ring radius (R) of 50 μm and straight arm length (L_c) of 120 μm. The waveguide width and height are 2.8 and 0.7 μm, respectively. The bus and ring wave guides are placed at a gap of 400 nm, which aids the operation in a slightly overcoupled regime [31]. The RMRR has a spectral filter enclosed within the ring waveguide. The practical realization of a spectral filter might be a Bragg grating similar to [53] inscribed within the lower straight arm of the resonator. The filter has a Gaussian profile with a spectral FWHM bandwidth denoted by, f as shown in the inset. The finite element method (FEM) is used to obtain the dispersion and nonlinear properties of the waveguide. Figure 3(b) shows the dispersion, D, and group velocity dispersion, β_2. The waveguide exhibits three zero dispersion wavelengths (ZDWs), namely, at 1040 nm, 1700 nm, and 2670 nm, respectively. The pump wavelengths used in this study are at 1029.7 nm and 1702.1 nm and are denoted by P1 and P2. Clearly, P1 and P2 are very close to the ZDWs, and the corresponding β_2 values are 22 ps^2/km and 25.9921 ps^2/km, respectively, at these wavelengths. The f is 10.475 nm and 11.166 nm at P1 and P2, respectively. The RMRR is pumped by a linearly chirped super-Gaussian pulse of the following
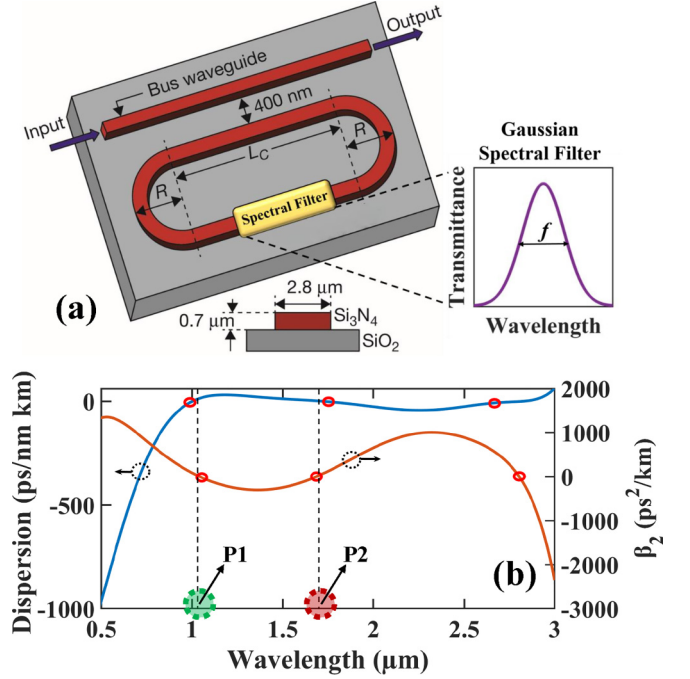

FIG. 3. (a) Schematic of the proposed RMRR with spectral filter, $R = 50$ μm, straight arm length, $L_c = 120$ μm. Inset shows the resonator cross section of waveguide. Spectral filter has a bandwidth f of ∼10 nm (at a pump wavelength of 1029.7 nm) and ∼11 nm (at a pump wavelength of 1702.1 nm). (b) Dispersion (D) and second-order GVD (β_2) (red circles correspond to the zero dispersion points; P1 and P2 denote the pump wavelengths).

form:

$$E_{\text{in}}(\tau) = E_{\text{in}} \exp\left[-\left(\frac{\tau^2}{2\tau_g^2}\right)^q - \frac{iC\tau^2}{2\tau_g^2} \right], \qquad (8)$$

where q and C are the super-Gaussian order and chirp parameters, respectively. The FWHM pulse width ($2\tau_g$) is 3.56 ps. The input pulse in the temporal domain is shown in Fig. 4(a). The DKS propagation in the present situation is numerically simulated by using the modified normalized LLE-F, which is

TABLE II. Simulation parameters for chirped DKS generation.

| Parameter	Value
Pump wavelength (λ_0)	1029.7 nm
Resonant wavelength (λ_R)	1029.98 nm
Round-trip time (t_R)	3.717 ps
Cavity detuning (δ_0)	0.2217 rad
Round-trip loss (α)	0.0019
Coupling coefficient ($\kappa_{\text{normalized}}$)	0.002938
Second-order GVD (β_2)	22 ps^2/km
Third-order dispersion (TOD) (β_3)	−0.198 ps^3/km
Nonlinear parameter (γ)	1.15 W^{-1}m^{-1}
Input power (P_{in})	100 mW
Desynchronization (Δt)	0.056 ps
Chirp (C)	0.3–0.75
Filter bandwidth (f)	10.475 nm
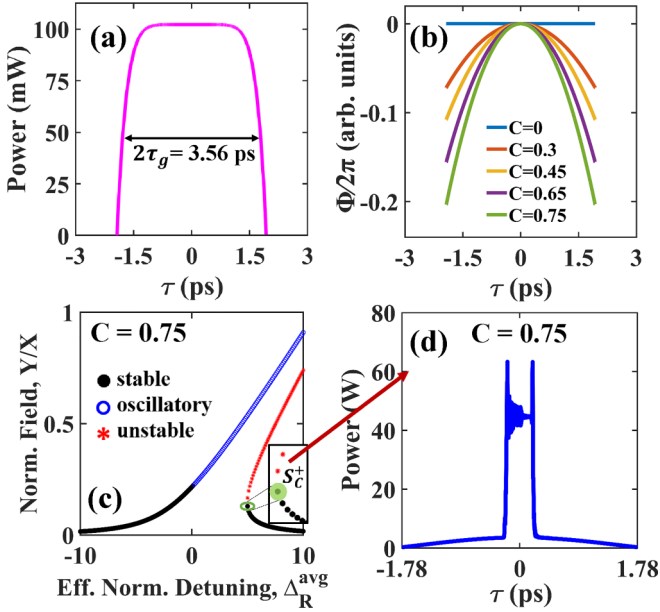
FIG. 4. (a) Temporal profile of the driving field ($2\tau_g$ represents the FWHM), (b) phase profile for different chirp values, (c) normalized tilt response corresponding to Eq. (17) (for real values of Δ_R^{avg} and α_R^{avg}), at a chirp, $C = 0.75$, where S_C^+ denotes the up-switching point, and (d) chirped temporal DKS state at S_C^+ obtained by solving Eq. (13) using parameters enlisted in Table II, at $C = 0.75$. Note that the chirped DKS develops on top of the driving field background.

given as

$$
\frac{\partial E'}{\partial t'} = \left[-1 + \left(-i + \frac{1}{\Omega^2} \right) \frac{\partial^2}{\partial \tau'^2} + i(|E'|^2 - D) - d\frac{\partial}{\partial \tau'} \right] E' + S(\tau'),
\tag{9}
$$

where

$$
S(\tau') = S_{\text{in}} e^{i\phi(\tau')},
\tag{10}
$$

$$
S_{\text{in}} = S_0 \, exp\left[-\left(\frac{\tau'^2}{2\tau_g'^2} \right)^q \right],
\tag{11}
$$

and

$$
\phi(\tau') = \frac{-C\tau'^2}{2\tau_g'^2}.
\tag{12}
$$

The value of C is chosen in the range 0.3–0.75 to aid in the generation of distortionless single-chirped DKS according to studies reported in [54]. The phase profile of the pump field as in Eq. (12) is shown in Fig. 4(b) for different chirp (C) values. It can be seen that at $C = 0$ the phase is zero and the phase profile is parabolic for all $C > 0$ values. As the value of C increases from 0.3 to 0.75 the slope of the phase profile becomes steeper at the leading and trailing edges of the input pulse.

By inserting $E' = E_0 e^{i\phi(\tau')}$ into Eq. (9) according to the procedure illustrated in [54], the following equation is

obtained:

$$
\frac{\partial E_0}{\partial t'} = \left\{ -\alpha_R + (i|E_0|^2 - \Delta_R) \right.
$$
$$
+ \left[2\left(1 + \frac{i}{\Omega^2} \right)\phi'(\tau') - d \right]\frac{\partial}{\partial \tau'}
$$
$$
\left. + \left(-i + \frac{1}{\Omega^2} \right)\frac{\partial^2}{\partial \tau'^2} \right\} E_0 + S_{\text{in}},
\tag{13}
$$

where

$$
\alpha_R = 1 - \left(1 + \frac{i}{\Omega^2} \right)\phi''(\tau')
\tag{14}
$$

and

$$
\Delta_R = D - \left(i - \frac{1}{\Omega^2} \right)[\phi'(\tau')]^2 + d\phi'(\tau').
\tag{15}
$$

α_R and Δ_R are the effective normalized τ' dependent loss and detuning [54], respectively.

B. Results

1. Quasi-HSS analysis: Comb self-stabilization

The normalized LLE, given in Eq. (13), is solved with the steady-state ($\frac{\partial E_0}{\partial t'}$) and homogeneous ($\frac{\partial E_0}{\partial \tau'}$) criteria and results in the cubic equation as stated in Eq. (16),

$$
X = (\alpha_R + \Delta_R)^2 Y - Y^3,
\tag{16}
$$

where $X = |(S_{\text{in}})_{\text{avg}}|^2$ and $Y = |E_0|^2$. Unlike Eq. (4) where there is no phase dependency of the detuning parameter, Eq. (16) contains Δ_R and α_R, which strictly depends on phase. Hence, this HSS equation is called the quasihomogeneous steady-state (Q-HSS) equation. Equation (16) also yields three intracavity field solutions: (1) stable, (2) unstable, and (3) oscillatory, like conventional HSS. Equation (16) resembles a second-order polynomial in effective normalized detuning Δ_R and is solved for the three sets of solutions as

$$
\Delta_R = -\alpha_R \pm \sqrt{Y^2 + \left(\frac{X}{Y} \right)}.
\tag{17}
$$

The condition $\frac{dX}{dY} = 0$ is applied to Eq. (16) to obtain

$$
Y_{\pm} = \pm \frac{\alpha_R + \Delta_R}{\sqrt{3}}.
\tag{18}
$$

Using Eqs. (16) and (18), the up-switching point X^+ or S_C^+ is obtained as

$$
X^+ = S_C^+ = \frac{2(\alpha_R + \Delta_R)^3}{3\sqrt{3}}.
\tag{19}
$$

The solution of Eq. (17) is referred to here as the quasi-HSS tilt response, which is plotted in Fig. 4(c) for the chirp $C = 0.75$, at a fixed pump wavelength of 1029.7 nm and over a range of real values of average effective detuning Δ_R^{avg}. Note that for a particular chirp value, the real part of average effective loss α_R^{avg} is unique. Here the black-filled circles, red asterisks, and blue open circles correspond to stable, unstable, and oscillatory solutions, respectively. At the up-switching point S_C^+ [marked in the magnified inset of

Fig. 4(c)], the intracavity stable single DKS field is shown in Fig. 4(d). Corresponding to this particular solution, the un-normalized detuning δ_0 is 0.2217 rad, which is calculated by FDTD numerical simulations for an input pump power P_{in} of 100 mW. All other necessary parameters have been summarized in Table II. Note that the spectral filter bandwidth f should be greater than the FSR of the cavity [55] (refer to the Appendix for details). The presence of any perturbing element within the MRR geometry such as grating [53] or air discontinuities [56] may generate a counterpropagating wave within the resonator [57], which can inherently give rise to either mode splitting or line-width broadening of the resonant peaks [58–60]. This might affect the intrinsic quality factor (Q factor) of the resonator and may further enhance the threshold for parametric oscillation [61]. However, the counterpropagating wave, in general, is quite weak and may yield minimal coupling of energy to the propagating signal and hence poor splitting of the resonant peaks [57]. If the coupling is optimally low, then the presence of a grating (which constitutes the filter) does not significantly deteriorate the intrinsic Q of the MRR [62]. Also, it has been observed for an anomalous dispersion silica toroid microcavity resonator that the formation of DKS is not degraded in the presence of weak coupling [63]. To ensure negligible splitting, the grating design can be tailored [58]. However, the realistic optimization of the filter design parameters is outside the scope of this work at present. Only the filter bandwidth is optimized, which might be sufficient to illustrate the spatiotemporal dynamics of chirped DKSs reported in this work.

As observed from Fig. 4(d), the chirped temporal DKS appears as a square pulse that sits on top of the quasiflat region (region within the temporal FWHM width) of the pump pulse background. The power of this pulse is greater than the bright oscillatory DKS depicted in Fig. 2. Moreover, the pulse duration is large as compared to the single stable DKS in the anomalous dispersion regime (Fig. 1). This implies a better overlap with the input pulsed "holding" pump field, and hence a higher extraction of energy from the pump field is possible. This inherently indicates a better pump-to-soliton conversion efficiency [64,65]. The square-shaped DKS exhibits characteristic oscillatory peaks at the leading and trailing edges as the slope of the input phase profile changes steeply at the pulse edges, and the chirp accumulation is high at these locations [see Fig. 4(b) and Eq. (12)]. A high chirp accumulation gives rise to the oscillatory peaks in temporal power profile. The characteristic square profile is attributed to the cumulative effect of chirp and spectral filtering, along with nonlinear phase accumulation in the normal dispersion regime [22,44,52]. The temporal chirped DKSs sitting on top of the quasiflat pulsed background [corresponding to stable single chirped solutions of Eq. (13)] at chirp C values of 0.3, 0.45, 0.65, and 0.75 are shown in Fig. 5(a). Figure 5(b) shows the magnified view of the DKS. As denoted by the encircled regions, the oscillatory structures become less pronounced with a decrease in chirp value. Figure 5(c) represents the field evolution, which confirms sustained single-chirped DKS pulse propagation and has oscillations in the pulse wings.

The simulated carrier envelope(s) of the Kerr frequency comb(s) (KFCs) corresponding to the DKS states is shown in
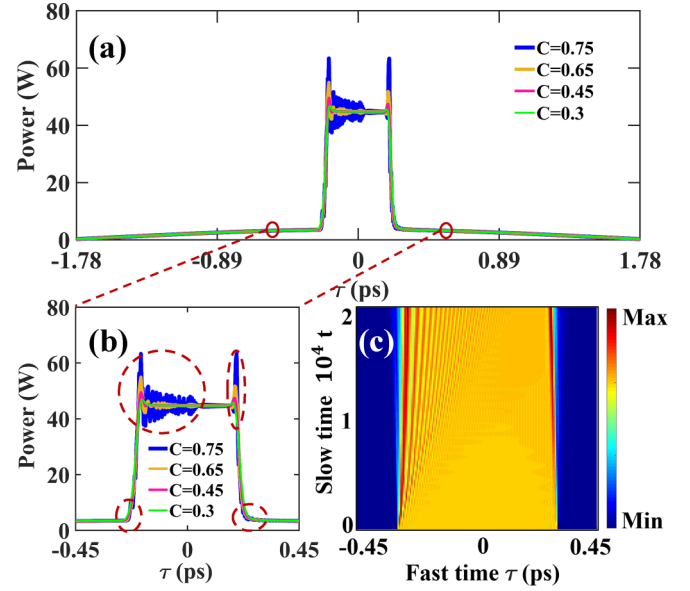

FIG. 5. (a) Temporal chirped DKS state at different chirp values, (b) enlarged view of the chirped DKS, where the encircled regions indicate the power fluctuation at the wings of the pulse due to phase accumulation, and (c) the steady-state field confinement at $C = 0.75$.

Fig. 6(a) for various values of $C = 0.3, 0.45, 0.65, 0.75$. The oscillatory structures in the pulse wings result in characteristic spectral side lobes in the KFCs, which have also been observed in [44] for Nyquist pulses and in [30] for single DKSs with multipeak temporal profiles, respectively, and in the normal dispersion regime. However, in the current work, the spectral side lobes are much more pronounced because
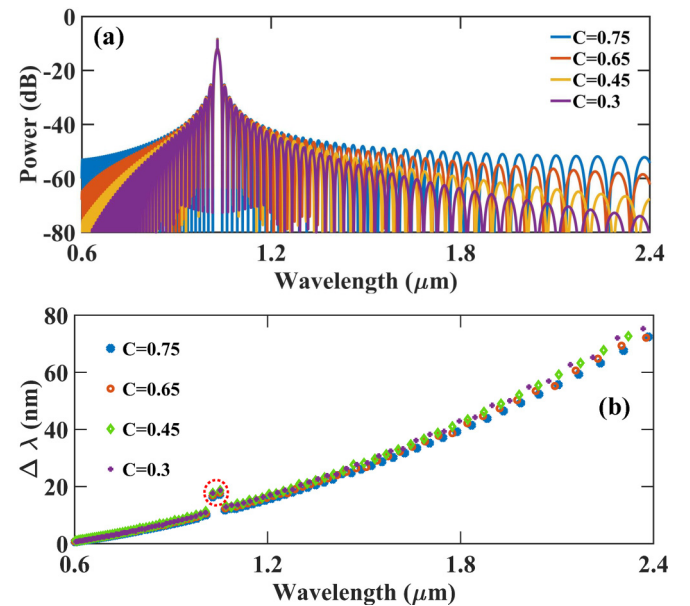

FIG. 6. (a) Carrier envelope of the frequency comb simulated from Eq. (13) for various chirp values; (b) spectral variation of $\Delta\lambda$, which is the wavelength shift of sub-comb-like signatures, for different chirp values (encircled combination correspond to frequency components close to the pump wavelength of 1029.7 nm).
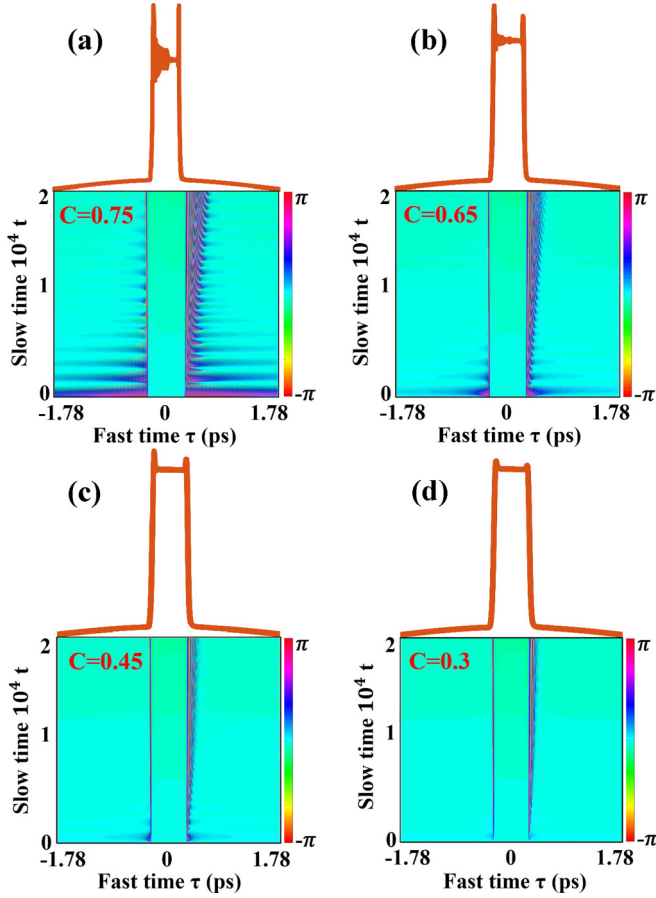
FIG. 7. Plot of round-trip phase accumulated over slow time t along the wings of the temporal chirped DKS state, (a) $C = 0.75$, (b) $C = 0.65$, (c) $C = 0.45$, and (d) $C = 0.3$. For the large chirp value, a significant oscillatory signature is seen.

of an effectively large nonlinear phase accumulation that is driven by the cumulative effect of input chirp, spectral filtering, nonlinearity, and normal dispersion. It is clear that the spectral side lobes, identified as sub-comb-like signatures, possess a characteristic wavelength shift, denoted as $\Delta\lambda$. The variation of $\Delta\lambda$ with wavelength has been plotted in Fig. 6(b). It is observed that $\Delta\lambda$ increases with an increase in wavelength.

To better understand the physics behind the unique signature of the chirped DKSs and their corresponding KFCs, we plot the evolution of the round-trip intracavity phase accumulated over the slow time (t) at $C = 0.75,\ 0.65,\ 0.45$, and 0.3 in Fig. 7. The respective DKS states are shown in the top. It can be seen that the phase accumulates along the wings of the pulse. The phase accumulated recursively over multiple round trips decreases with a decrease in the chirp value. This confirms the oscillatory peaks in the pulse wings and the sub-comb-like signatures manifest as a result of intracavity phase accumulation, aided by an input chirp.

The quasi-HSS tilt response obtained from Eq. (17) for the stable (black-filled circles), oscillatory (blue open circles), and unstable (red asterisks) solutions corresponding to $C = 0.3,\ 0.45,\ 0.65$, and 0.75 are shown in Figs. 8(a)–8(d), respectively. The lowermost branch of the tilt response, which
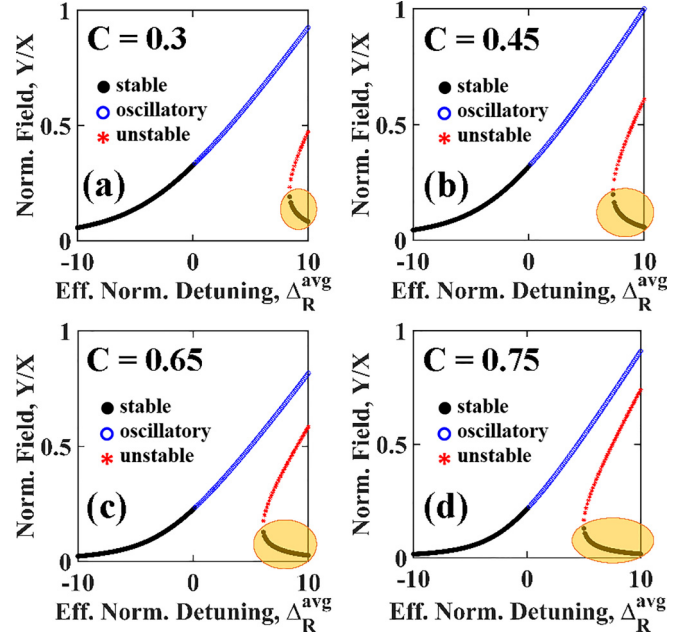

FIG. 8. Solution of the quasi-HSS tilt equation [Eq. (17)], considering the real values of Δ_R^{avg} and α_R^{avg}, for the stable (black filled circles), unstable (red asterisks), and oscillatory (blue open circles) solutions for various chirp values, (a) 0.3, (b) 0.45, (c) 0.65, and (d) 0.75. The shaded region in all four images indicates stable single-chirped DKS solutions.

governs the solutions for a stable single DKS state [shaded region(s) in Fig. 8], is pronounced with an increase in C. Thus, based on the quasi-HSS analysis, we can conclude that the input chirp parameter leads to a higher possibility of generating a stable single DKS state. From Fig. 8 it is also clear that multiple soliton states coexist for the same detuning, and the possibility of such coexistence increases with an increase in the magnitude of chirp. This behavior of chirped DKS is consistent with previous studies on bright and dark DKSs in the normal dispersion regime [30,66]. Note that effective detuning, Δ_R^{avg} values larger than the range plotted in Fig. 8 may yield the maximum peak in tilt response. However, this might result into unrealistic detuning (D and δ_0) values, not favoring the DKS generation [15].

2. Ikeda-F analysis

To corroborate our findings reported in the previous section, we present simulations from the Ikeda-F map [52] in the present section. Fundamentally distinct from the LLE, the Ikeda model [42] isolates the computation in two steps: (1) the propagation of the intracavity field envelope E inside the ring waveguide of an MRR over a single round trip and (2) the periodic boundary condition that caters to the coherent injection of the pulsed driving field into the MRR. Intracavity field evolution over a single round trip is governed by the well-known nonlinear Schrödinger equation (NLSE) as

$$\frac{\partial E}{\partial z} = -i\frac{\beta_2}{2}\frac{\partial^2 E}{\partial \tau^2} + i\gamma|E|^2 E, \qquad (20)$$

where E is the slowly varying intracavity field envelope, τ denotes the time in the moving frame of reference, and γ is the

TABLE III. Parameters for Ikeda-F simulation.

Parameter	Value
Pump wavelength (λ_0)	1702.1 nm
Resonant wavelength (λ_R)	1702.32 nm
Round-trip time (t_R)	3.6796 ps
Cavity detuning (δ_0)	1.0532 rad
Round-trip loss (α)	0.0117
Coupling coefficient ($\kappa_{\text{normalized}}$)	0.01278
Second-order GVD (β_2)	25.9921 ps^2/km
Nonlinear parameter (γ)	0.52084 W^{-1}m^{-1}
Input power (P_{in})	96 mW
Desynchronization (Δt)	0.0186 ps
Chirp (C)	0.3–0.75
Filter bandwidth (f)	11.166 nm

nonlinear parameter per unit length. The periodic boundary condition that describes the coherent addition of the chirped pulsed-pump field to the ring waveguide while incorporating the effects of loss and spectral filter can be written in the Fourier domain as

$$E_{n+1}(\omega) = e^{-i\delta_0}E_n(\omega)\left(\exp\left\{-\left[\frac{(\omega-\omega_0)^2}{f^2}\right.\right.\right.$$
$$\left.\left.\left.+\left(\frac{\alpha+\kappa}{2}\right)\right]\right\}\right) + E_{\text{in}}(\omega)\delta(\omega-\omega_0), \quad (21)$$

where $E_{\text{in}}(\omega) = \mathcal{F}\{E_{\text{in}}(\tau)\}$ is the chirped pump pulse in the frequency domain [$E_{\text{in}}(\tau)$ is the same as in Eq. (8)], $E_{n+1}(\omega)$ and $E_n(\omega)$ are the spectral fields at the beginning of the $(n+1)$th and end of nth round trips, respectively, and the other symbols have their usual meanings as given earlier.

The Ikeda-F simulations have been carried out at $C = 0.75$ and a pump wavelength (λ_0) of 1702.1 nm where the GVD β_2 is 25.9921 ps^2/km. All other parameters are listed in Table III. The chirped DKS state obtained from Ikeda-F simulation is shown in Fig. 9(a). The temporal profile exhibits oscillatory peaks in the leading and trailing edges of the pulse, similar to LLE-F. The simulated carrier envelope of the KFC is given in Fig. 9(b), which also contains spectral side lobes like Fig. 6(a). The subtle differences between the temporal and spectral signatures observed from LLE-F and Ikeda-F methods are probably because the loss and detuning definitions are included in different manners. The LLE is solved by including effective loss and detuning which consists of additional phase terms, but Ikeda-F is solved directly. The wavelength shift ($\Delta\lambda$) between the sub-comb-like signatures, as observed in the frequency comb, is plotted in Fig. 9(c), for both LLE-F and Ikeda-F approaches at $\lambda_0 = 1702.1$ nm. A reasonably good match between the two methods is visible.

3. τ-trapping position of generated chirped DKS

It has been demonstrated in [42] that in the case of pulsed driving, the intracavity DKS within a resonator is highly probable to experience an offset temporally from the driving pulse center. All such temporal locations, on top of the driving pulse background at which the DKS is robustly trapped, are referred to as the trapping fast time position τ_{trap}. The specific
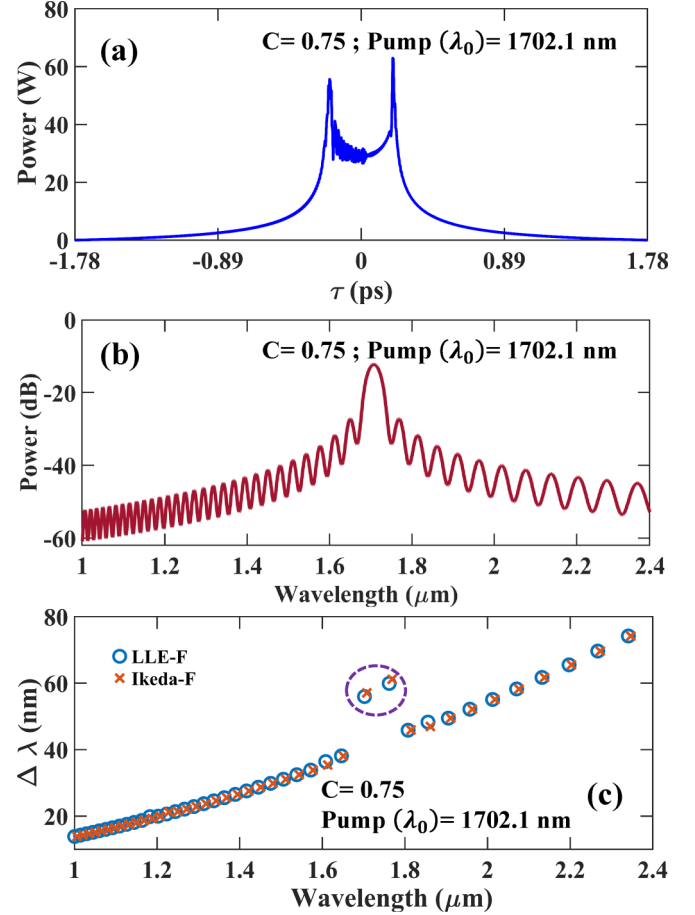

FIG. 9. Solution of Ikeda-F with chirped input at a pump wavelength ($\lambda_0 = 1702.1$ nm). (a) Temporal chirped DKS state, (b) carrier envelope of the frequency comb, and (c) comparison of $\Delta\lambda$ for the LLE-F and Ikeda-F formulations (encircled combination correspond to frequency components close to the pump wavelength).

τ_{trap} temporal locations that are away from the driving pulse center are determined by the driving pulse parameters [42,54]. This phenomenon of robust trapping of generated DKSs at temporally offset positions from the driving pulse center is known as spontaneous symmetry breaking (SSB) [42]. It has been shown that for a chirped driving pulse, the DKS is relocated to the center of the driving pulse after a critical chirp is attained [43,54]. This phenomenon has been referred to as SSB recovery [54]. In the case of our work, where the DKS experiences both a spectral filtering effect and chirping within a normal dispersion regime, we deduce that the SSB recovery occurs at a much lower critical chirp value. The LLE-F simulations in this section are performed according to the procedure described in [43]. The initial DKS position (τ_0) is fixed at 0.5 ps. Numerical simulations are carried out by sweeping the chirp value from 0 to 1. The total drift velocity v_{drift} of the DKS relative to the chirped super-Gaussian pulse is calculated according to the following expression [64]:

$$v_{\text{drift}} = a(S_0, \Delta_R^{\text{avg}})\phi'(\tau_0) + \cdots$$
$$+ b(S_0, \Delta_R^{\text{avg}})\{\text{Re}[S(\tau)]\}'\tau_0 + d, \quad (22)$$

where the coefficients a and b stem from the projection of the DKS's neutral mode [41,64] along a linear fast-time variation,
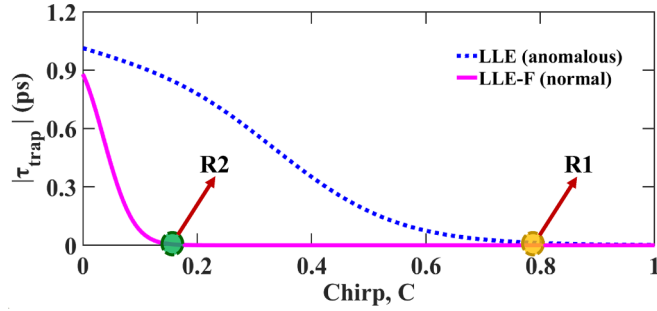
FIG. 10. Soliton trapping with respect to the fast time position (τ_{trap}) for various chirp parameters. Soliton trapping for both anomalous and normal dispersion regimes is shown and compared, where the positively chirped super-Gaussian input is considered according to [43]. R1 and R2 denote the points of SSB recovery. In the case of a normal dispersion regime (i.e., the present work), SSB recovery occurs at a much smaller value of the chirp parameter.

determined by S_0 and Δ_R^{avg}. The trapping locations, τ_{trap}, of the DKSs on top of the super-Gaussian background are shown in Fig. 10 (magenta curve). Note that all simulations corresponding to τ_{trap} for chirped DKS have been carried out at the up-switching point of the quasi-HSS response. The dotted blue line depicts τ_{trap} for the anomalous dispersion regime without spectral filtering according to [43], which is plotted for the sake of comparison. R1 and R2 denote the critical values of chirp for SSB recovery [42], i.e., the values of chirp at which $\tau_{\text{trap}} = 0$. Initially for $C = 0$, a DKS located at $\tau_0 = 0.5$ is delayed from the center zero of the background and reaches a stable trapping position at the trailing edge of the driving pulse. This is true for both normal and anomalous dispersion schemes. With an increase in C, the DKS experiences a delay for the anomalous dispersion situation, with a reduced rate till it reaches point R1 at $C = 0.78$, as visible from the slope of the curve (dotted blue curve). At this position, the DKS accelerates to the central peak of the driving super-Gaussian background until τ symmetry is completely recovered. However, in the case of a normal dispersion regime, the SSB recovery point R2 occurs at $C = 0.16$. Therefore, the combination of spectral filtering and input chirp in the normal dispersion regime facilitates stable trapping of the generated chirped DKS at a much lower positive chirp value. In addition, as $C > 0$ in the present work, the chirped DKS is trapped at the stable $\tau_{\text{trap}} = 0$ position of the up-switching point.

IV. CONCLUSION

To conclude the work, we have proposed a scheme to achieve a stable bright DKS state and corresponding KFC in the normal dispersion regime. The combination of a super-Gaussian chirped pulsed pump along with spectral filtering and normal dispersion of the waveguide that constitute the racetrack microring resonator produces a unique square-shaped temporal signature of the output pulses. The characteristic square shape leads to better temporal overlap with the holding pulsed driving field. Extensive analytical and numerical formulations through the quasi-HSS and LLE-F equations, respectively, have indicated that chirped pulsed pumping facilitates the sustained single DKS
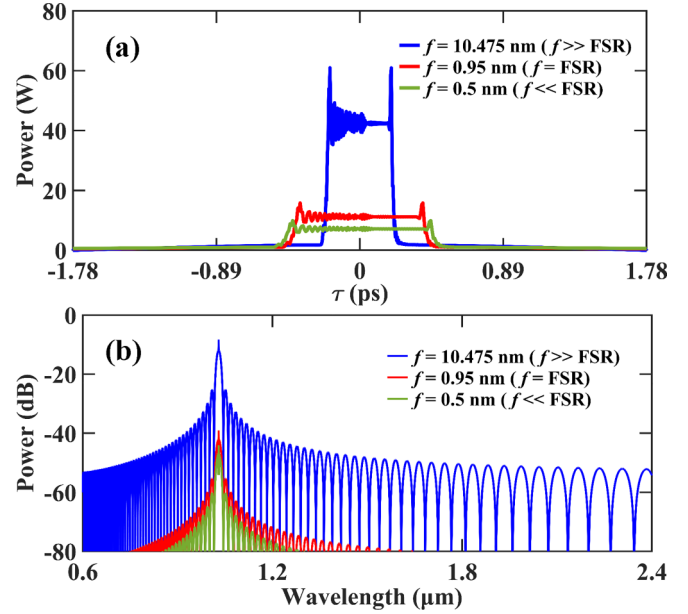

FIG. 11. (a) Chirped temporal DKS and (b) corresponding carrier envelope of frequency comb for different spectral filter bandwidth f. Three cases for $f \gg$ FSR ($f = 10.475$ nm), $f =$ FSR ($f = 0.95$ nm), and $f \ll$ FSR ($f = 0.5$ nm) have been depicted.

operation regime. The studies through LLE-F have been validated through the modified Ikeda model. We also observe that SSB recovery occurs at a low chirp value in the present scheme as compared to the anomalous dispersion situation. It should also be pointed out that, although this work has been carried out at small nonzero desynchronization (Δt) values, $\Delta t = 0$ also yields similar spectro-temporal characteristics.

APPENDIX: DEPENDENCE OF SPECTRAL FILTER BANDWIDTH f ON FSR OF CAVITY

Figure 11 depicts how the bandwidth of the spectral filter affects the spectro-temporal characteristics of the resonator for a fixed FSR, such as $f \gg$ FSR, $f =$ FSR, $f \ll$ FSR at a fixed pump wavelength, $\lambda_0 = 1029.7$ nm. The FSR of the resonator is 0.95 nm at the pump wavelength. It is observed that when the spectral bandwidth is much larger than the FSR, i.e., $f \gg$ FSR, the temporal DKS has the largest power and wide KFC spectral bandwidth, whereas for $f =$ FSR (i.e., $f = 0.95$ nm) and $f \ll$ FSR (i.e., $f = 0.5$ nm), the power of the DKS reduces and the spectral bandwidth of the KFC also decreases. The decrease in the spectral bandwidth manifests as an increase in the temporal width of the DKS. Such behavior resulting in the enhanced frequency comb bandwidth with an increase in spectral filter bandwidth has also been reported in recent studies [22,67].

[1] M. Saha, S. Roy, and S. K. Varshney, Phys. Rev. A **101**, 033826 (2020).

[2] T. J. Kippenberg, R. Holzwarth, and S. A. Diddams, Science **332**, 555 (2011).

[3] P. Del'Haye, A. Schliesser, O. Arcizet, T. Wilken, R. Holzwarth, and T. J. Kippenberg, Nature (London) **450**, 1214 (2007).

[4] A. Roy, R. Haldar, and S. K. Varshney, J. Light. Technol. **36**, 5807 (2018).

[5] M. Saha, S. Roy, and S. K. Varshney, Phys. Rev. E **100**, 022201 (2019).

[6] G. Moille, X. Lu, A. Rao, Q. Li, D. A. Westly, L. Ranzani, S. B. Papp, M. Soltani, and K. Srinivasan, Phys. Rev. Appl. **12**, 034057 (2019).

[7] A. Pasquazi, M. Peccianti, L. Razzari, D. J. Moss, S. Coen, M. Erkintalo, Y. K. Chembo, T. Hansson, S. Wabnitz, P. Del'Haye *et al.*, Phys. Rep. **729**, 1 (2018).

[8] P. Grelu and N. Akhmediev, Nat. Photonics **6**, 84 (2012).

[9] T. J. Kippenberg, A. L. Gaeta, M. Lipson, and M. L. Gorodetsky, Science **361**, eaan8083 (2018).

[10] R. Holzwarth, Th. Udem, T. W. Hänsch, J. C. Knight, W. J. Wadsworth, and P. St. J. Russell, Phys. Rev. Lett. **85**, 2264 (2000).

[11] D. T. Spencer, T. Drake, T. C. Briles, J. Stone, L. C. Sinclair, C. Fredrick, Q. Li, D. Westly, B. R. Ilic, A. Bluestone *et al.*, Nature (London) **557**, 81 (2018).

[12] F. Leo, S. Coen, P. Kockaert, S.-P. Gorza, P. Emplit, and M. Haelterman, Nat. Photonics **4**, 471 (2010).

[13] A. Foltynowicz, P. Masłowski, T. Ban, F. Adler, K. Cossel, T. Briles, and J. Ye, Farad. Disc. **150**, 23 (2011).

[14] J. K. Jang, M. Erkintalo, S. Coen, and S. G. Murdoch, Nat. Commun. **6**, 7370 (2015).

[15] S. Kar, M. Saha, S. K. Bag, R. K. Sinha, S. Sharma, S. Singhal, and S. K. Varshney, Phys. Rev. A **106**, 013517 (2022).

[16] T. Herr, V. Brasch, J. D. Jost, C. Y. Wang, N. M. Kondratiev, M. L. Gorodetsky, and T. J. Kippenberg, Nat. Photonics **8**, 145 (2014).

[17] Y. Wang, M. Anderson, S. Coen, S. G. Murdoch, and M. Erkintalo, Phys. Rev. Lett. **120**, 053902 (2018).

[18] S. Kelly, Electron. Lett. **28**, 1562 (1992).

[19] H. A. Haus and W. S. Wong, Rev. Mod. Phys. **68**, 423 (1996).

[20] A. Chong, J. Buckley, W. Renninger, and F. Wise, Opt. Express **14**, 10095 (2006).

[21] S.-W. Huang, H. Zhou, J. Yang, J. F. McMillan, A. Matsko, M. Yu, D.-L. Kwong, L. Maleki, and C. W. Wong, Phys. Rev. Lett. **114**, 053901 (2015).

[22] C. Spiess, Q. Yang, X. Dong, V. G. Bucklew, and W. H. Renninger, Optica **8**, 861 (2021).

[23] X. Xue, Y. Xuan, Y. Liu, P.-H. Wang, S. Chen, J. Wang, D. E. Leaird, M. Qi, and A. M. Weiner, Nat. Photonics **9**, 594 (2015).

[24] C. Bao, Y. Xuan, C. Wang, A. Fülöp, D. E. Leaird, V. Torres-Company, M. Qi, and A. M. Weiner, Phys. Rev. Lett. **121**, 257401 (2018).

[25] B. Garbin, Y. Wang, S. G. Murdoch, G.-L. Oppo, S. Coen, and M. Erkintalo, Eur. Phys. J. D **71**, 240 (2017).

[26] Y. Xu, A. Sharples, J. Fatome, S. Coen, M. Erkintalo, and S. G. Murdoch, Opt. Lett. **46**, 512 (2021).

[27] P. Parra-Rivas, S. Coulibaly, M. G. Clerc, and M. Tlidi, Phys. Rev. A **103**, 013507 (2021).

[28] M. G. Clerc, S. Coulibaly, P. Parra-Rivas, and M. Tlidi, Chaos **30** (2020).

[29] M. Liu, H. Huang, Z. Lu, Y. Dang, S. Mei, C. Wang, B. Zhao, and W. Zhao, Phys. Rev. Appl. **18**, 044028 (2022).

[30] Z. Li, Y. Xu, S. Coen, S. G. Murdoch, and M. Erkintalo, Optica **7**, 1195 (2020).

[31] J. K. Jang, A. Klenner, X. Ji, Y. Okawachi, M. Lipson, and A. L. Gaeta, Nat. Photonics **12**, 688 (2018).

[32] H. Guo, M. Karpov, E. Lucas, A. Kordts, M. H. Pfeiffer, V. Brasch, G. Lihachev, V. E. Lobanov, M. L. Gorodetsky, and T. J. Kippenberg, Nat. Phys. **13**, 94 (2017).

[33] X. Yi, Q.-F. Yang, K. Y. Yang, and K. Vahala, Opt. Lett. **41**, 2037 (2016).

[34] H. Taheri, A. A. Eftekhar, K. Wiesenfeld, and A. Adibi, IEEE Photonics J. **7**, 1 (2015).

[35] X. Xue, X. Zheng, and B. Zhou, Photonics Res. **6**, 948 (2018).

[36] J. Pan, Z. Cheng, T. Huang, C. Song, P. P. Shum, and G. Brambilla, J. Light. Technol. **37**, 5531 (2019).

[37] C. Bao, L. Zhang, A. Matsko, Y. Yan, Z. Zhao, G. Xie, A. M. Agarwal, L. C. Kimerling, J. Michel, L. Maleki *et al.*, Opt. Lett. **39**, 6126 (2014).

[38] X. Xue, P.-H. Wang, Y. Xuan, M. Qi, and A. M. Weiner, Laser Photonics Rev. **11**, 1600276 (2017).

[39] X. Xue, X. Zheng, and B. Zhou, Nat. Photonics **13**, 616 (2019).

[40] E. Obrzud, S. Lecomte, and T. Herr, Nat. Photonics **11**, 600 (2017).

[41] I. Hendry, B. Garbin, S. G. Murdoch, S. Coen, and M. Erkintalo, Phys. Rev. A **100**, 023829 (2019).

[42] I. Hendry, W. Chen, Y. Wang, B. Garbin, J. Javaloyes, G.-L. Oppo, S. Coen, S. G. Murdoch, and M. Erkintalo, Phys. Rev. A **97**, 053834 (2018).

[43] F. R. Talenti, Y. Sun, P. Parra-Rivas, T. Hansson, and S. Wabnitz, Opt. Commun. **546**, 129773 (2023).

[44] X. Xue, P. Grelu, B. Yang, M. Wang, S. Li, X. Zheng, and B. Zhou, Light Sci. Appl. **12**, 19 (2023).

[45] L. A. Lugiato and R. Lefever, Phys. Rev. Lett. **58**, 2209 (1987).

[46] P. Grelu, *Nonlinear Optical Cavity Dynamics: From Microresonators to Fiber Lasers* (John Wiley & Sons, New York, 2015).

[47] S. Coen, H. G. Randle, T. Sylvestre, and M. Erkintalo, Opt. Lett. **38**, 37 (2013).

[48] G. P. Agrawal, in *Nonlinear Science at the Dawn of the 21st Century*, edited by P. L. Christiansen, M. P. Srensen, and A. C. Scott, Lecture Notes in Physics Vol. 542 (Springer, Berlin, Heidelberg, 2000), pp. 195–211.

[49] C. Godey, I. V. Balakireva, A. Coillet, and Y. K. Chembo, Phys. Rev. A **89**, 063814 (2014).

[50] A. Coillet, I. Balakireva, R. Henriet, K. Saleh, L. Larger, J. M. Dudley, C. R. Menyuk, and Y. K. Chembo, IEEE Photonics J. **5**, 6100409 (2013).

[51] P. Parra-Rivas, E. Knobloch, D. Gomila, and L. Gelens, Phys. Rev. A **93**, 063839 (2016).

[52] X. Dong, C. Spiess, V. G. Bucklew, and W. H. Renninger, Phys. Rev. Res. **3**, 033252 (2021).

[53] A. Arbabi, Y. M. Kang, C.-Y. Lu, E. Chow, and L. L. Goddard, Appl. Phys. Lett. **99**, 091105 (2011).

[54] J. Pan, C. Xu, Z. Wu, J. Zhang, T. Huang, and P. P. Shum, Front. Optoelectron. **15**, 14 (2022).

[55] M. Peccianti, A. Pasquazi, Y. Park, B. E. Little, S. T. Chu, D. J. Moss, and R. Morandotti, Nat. Commun. **3**, 765 (2012).

[56] S. K. Bag and S. K. Varshney, J. Opt. Soc. Am. B **38**, 1669 (2021).

[57] M.-Y. Ye, M.-X. Shen, and X.-M. Lin, Sci. Rep. **7**, 17412 (2017).

[58] Q. Huang, K. Ma, and S. He, IEEE Photonics Technol. Lett. **27**, 1402 (2015).

[59] Y. Zhi, X.-C. Yu, Q. Gong, L. Yang, and Y.-F. Xiao, Adv. Mater. **29**, 1604920 (2017).

[60] S. K. Bag, R. K. Sinha, M. Wan, and S. Varshney, J. Phys. D **54**, 16LT01 (2021).

[61] X. Yi, Q.-F. Yang, K. Y. Yang, M.-G. Suh, and K. Vahala, Optica **2**, 1078 (2015).

[62] Z. Zhang, M. Dainese, L. Wosinski, and M. Qiu, Opt. Express **16**, 4621 (2008).

[63] S. Fujii, A. Hori, T. Kato, R. Suzuki, Y. Okabe, W. Yoshiki, A.-C. Jinnai, and T. Tanabe, Opt. Express **25**, 28969 (2017).

[64] M. Erkintalo, S. G. Murdoch, and S. Coen, J. R. Soc. N. Z. **52**, 149 (2022).

[65] J. Li, C. Bao, Q.-X. Ji, H. Wang, L. Wu, S. Leifer, C. Beichman, and K. Vahala, Optica **9**, 231 (2022).

[66] P. Parra-Rivas, D. Gomila, and L. Gelens, Phys. Rev. A **95**, 053863 (2017).

[67] Y. Yu, Z. Wang, Z. Fang, Y. Li, and Z. Zhang, Phys. Rev. A **108**, 053505 (2023).